

# Magicity and occurrence of band with enhanced $B(E2)$ in neutron-rich nuclei $^{68}\text{Ni}$ and $^{90}\text{Zr}$

K. Kaneko,<sup>1</sup> M. Hasegawa,<sup>2</sup> T. Mizusaki,<sup>3,4</sup> and Y. Sun<sup>5,6,7</sup>

<sup>1</sup>*Department of Physics, Kyushu Sangyo University, Fukuoka 813-8503, Japan*

<sup>2</sup>*Laboratory of Physics, Fukuoka Dental College, Fukuoka 814-0193, Japan*

<sup>3</sup>*Institute of Natural Sciences, Senshu University, Kawasaki, Kanagawa, 214-8580, Japan*

<sup>4</sup>*Center for Nuclear Study (CNS), University of Tokyo,  
Wako Campus of RIKEN, Wako 351-0198, Japan*

<sup>5</sup>*Department of Physics and Joint Institute for Nuclear Astrophysics,  
University of Notre Dame, Notre Dame, IN 46556, USA*

<sup>6</sup>*Department of Physics, Tsinghua University, Beijing 100084, P. R. China*

<sup>7</sup>*Department of Physics, Xuzhou Normal University, Xuzhou, Jiangsu 221009, P. R. China*

(Dated: September 30, 2018)

Experimental energy spectrum and  $B(E2)$  values in  $^{68}\text{Ni}$  and  $^{90}\text{Zr}$  indicate a double-magic character in these neutron-rich nuclei with  $N$  or  $Z = 40$ . The data nevertheless do not show any pronounced irregularity in two-nucleon separation energy. To understand the underlying physics, we carry out both shell-model and mean-field calculations. The shell-model calculation can well reproduce all the observations. It is understood from the mean-field results for  $^{68}\text{Ni}$  that the shell gap at  $N = 40$  disappears due to dynamical correlations of the isovector  $J = 0$  pairing interaction. In  $^{90}\text{Zr}$ , however, such a dynamic process with the  $J = 0$  pairing appears not important because of the strong contribution of the  $J > 0$  interaction. We study also level schemes in the Ni isotopes and  $N = 50$  isotones. We predict a new band built on the  $0_2^+$  state in both  $^{68}\text{Ni}$  and  $^{90}\text{Zr}$ . The states of this band are dominated by two-particle-two-hole excitations from the  $fp$ -shell to the intruder  $g_{9/2}$  orbit.

PACS numbers: 21.10.Dr, 21.60.Cs, 21.60.Jz, 21.10.Re

## I. INTRODUCTION

The study of nuclear shell effects away from the valley of stability is one of the current topics in nuclear structure physics. The most interesting aspects are how the well-known shell effects, such as the occurrence of magic numbers [1] and the shape-coexistence phenomenon [2, 3], manifest themselves in exotic mass regions where nuclei have unusual combinations of neutron and proton number. There have been intensive discussions on the issue of weakening of shell effect in neutron-rich nuclei. For example, the spherical  $N = 20$  shell gap for light nuclei disappears in neutron-rich isotopes, leading to strongly deformed ground states and large  $E2$  transition probabilities between the  $2_1^+$  state and ground state ( $0_1^+$ ). By using the shell-model approach, it has been demonstrated [4] that the magic number at  $N = 20$  vanishes due to the proton-neutron attraction between spin-orbit partners of maximum  $j$ . On the other hand, there have been suggestions [5] that the strong deformation effects around  $^{32}\text{Mg}$  are induced by dynamical correlations, such as the neutron pairing correlations.

It has been found [6, 7, 8, 9] by several experiments that the neutron-rich nucleus  $^{68}\text{Ni}$  ( $Z = 28, N = 40$ ) shows a double-magic character: a relatively large  $2_1^+$  excitation energy and a small  $B(E2, 0_1^+ \rightarrow 2_1^+)$  value, which is comparable to the cases of double-magic nuclei  $^{16}\text{O}$ ,  $^{40}\text{Ca}$ , and  $^{48}\text{Ca}$ . The nucleus  $^{68}\text{Ni}$  lies far from the neutron drip line, and the neutron energy gap between the  $fp$ -shell and the  $g_{9/2}$  intruder orbit appears to be sizeable at  $N = 40$ . It was discussed in Ref. [10, 11] that

in the early mean-field calculations, a distinct shell gap that exists in the  $N = 40$  nucleus  $^{68}\text{Ni}$  disappears when quadrupole correlations are taken into account. For  $^{68}\text{Ni}$ , it is remarkable that this nucleus does not show a pronounced irregularity in two-neutron separation energy, as expected for a typical double-magic nucleus. It was suggested [12] that small  $B(E2, 0_1^+ \rightarrow 2_1^+)$  value is not a strong evidence for the double-magic character. We may thus conclude that the double-magicity nature in  $^{68}\text{Ni}$  is still controversial and remains an open question.

In general, shell closure leads to spherical configurations for the ground state, while breaking of a magic shell can produce coexisting deformed states. An important indication for the emergent deformation is the appearance of low-lying  $0^+$  bands. The deformed structure occurs as a consequence of nuclear correlations, which excite nucleons from the closed shell to a higher shell. For example, the typical double-magic nucleus  $^{56}\text{Ni}$  ( $Z = N = 28$ ) [13, 14, 15] is known to have two collective bands with large deformations coexisting with the spherical ground band. Therefore, it is very interesting to examine theoretically whether such collective bands exist also in  $^{68}\text{Ni}$ .

Similar discussions would also apply to the neutron-rich nucleus  $^{90}\text{Zr}$ , which has a closed  $Z = 40$  proton subshell and a strong  $N = 50$  neutron shell closure. This is an interesting case to study the persistence of the  $Z = 40$  stability. Recently, energy levels and  $B(E2)$  values in  $^{90}\text{Zr}$  have been measured [16], which showed a double magic character: a relatively large  $2_1^+$  excitation energy and a small  $B(E2, 0_1^+ \rightarrow 2_1^+)$  value. However, this nu-

cleus does not indicate a pronounced irregularity in two-proton separation energy. Moreover, it is known that a low-lying  $0_2^+$  state exists at  $Z = 40$  in the  $N = 50$  isotonic chain. Hence we can expect to see excited bands in  $^{90}\text{Zr}$  but perhaps with different structure.

In this paper, we study the magicity at  $N$  or  $Z = 40$  and structure of excited  $0_2^+$  bands in the neutron-rich nuclei  $^{68}\text{Ni}$  and  $^{90}\text{Zr}$ . To understand the physics in a systematical way, we perform spherical shell-model calculations for the Ni isotopes and  $N = 50$  isotones. Conventional shell-model calculations in the  $(1f_{7/2}, 2p_{3/2}, 1f_{5/2}, 2p_{1/2}, 1g_{9/2})$  shell space for  $N, Z = 30 - 36$  are not possible at present because of the huge dimension of configuration space; we need to restrict the model space to the  $2p_{3/2}, 1f_{5/2}, 2p_{1/2}$ , and  $1g_{9/2}$  orbitals (hereafter called the *fp**g*-shell). Of course, neutron (proton) excitations from the  $1f_{7/2}$  orbit to the *fp**g*-shell cannot be neglected for  $^{68}\text{Ni}$  ( $^{90}\text{Zr}$ ) [9, 11]. Nevertheless, after all we shall see that the variations in  $B(E2)$  in the nuclei around  $^{68}\text{Ni}$  ( $^{90}\text{Zr}$ ) can be understood in terms of valence neutrons (protons) in this restricted model space. For the Ni isotopes, we employ an effective interaction starting from a realistic neutron G-matrix interaction based on the Bonn-C *NN* potential (called VMS interaction) [17]. For the  $N = 50$  isotones, we use two types of effective interactions: the proton part of the VMS interaction and the effective interaction of Ji and Wildenthal (called JW interaction) [18].

The paper is arranged as follows. In Sections II and III, we present the numerical calculations and discuss the results for Ni isotopes and  $N = 50$  isotones, respectively. Conclusions are drawn in Sec. IV.

## II. NI ISOTOPES

### A. Magicity in $^{68}\text{Ni}$

Let us first review what the experiment has found for the Ni isotopes. In Fig. 1, the experimental  $B(E2, 0_1^+ \rightarrow 2_1^+)$  value and the first excited  $2_1^+$  energy are shown as a function of neutron number  $N$  for  $^{58-70}\text{Ni}$ . With increasing  $N$ ,  $B(E2)$  decreases quickly and becomes the smallest at  $N = 40$ . In contrast, changes in the  $2_1^+$  energy ( $E_{2_1^+}$ ) are quite small for  $^{58-66}\text{Ni}$ , but  $E_{2_1^+}$  jumps to a large value at  $N = 40$ . Thus, with a pronounced large  $E_{2_1^+}$  and a small  $B(E2, 0_1^+ \rightarrow 2_1^+)$ , these data seem to suggest a subshell closure at  $N = 40$  in  $^{68}\text{Ni}$ .

We now carry out shell-model calculations for the Ni isotopes. The shell-model Hamiltonian is written as

$$H = \sum_{\alpha} \varepsilon_{\alpha} c_{\alpha}^{\dagger} c_{\alpha} + \frac{1}{4} \sum_{\alpha\beta\gamma\delta} V_{\alpha\beta,\gamma\delta} c_{\alpha}^{\dagger} c_{\beta}^{\dagger} c_{\delta} c_{\gamma}, \quad (1)$$

where  $\varepsilon_{\alpha}$  are single-particle energies and  $V_{\alpha\beta,\gamma\delta}$  two-body matrix elements. Since  $^{56}\text{Ni}$  is taken as a core, the model space is restricted to the *fp**g*-shell for neutrons and protons are assumed to be inactive. The proton

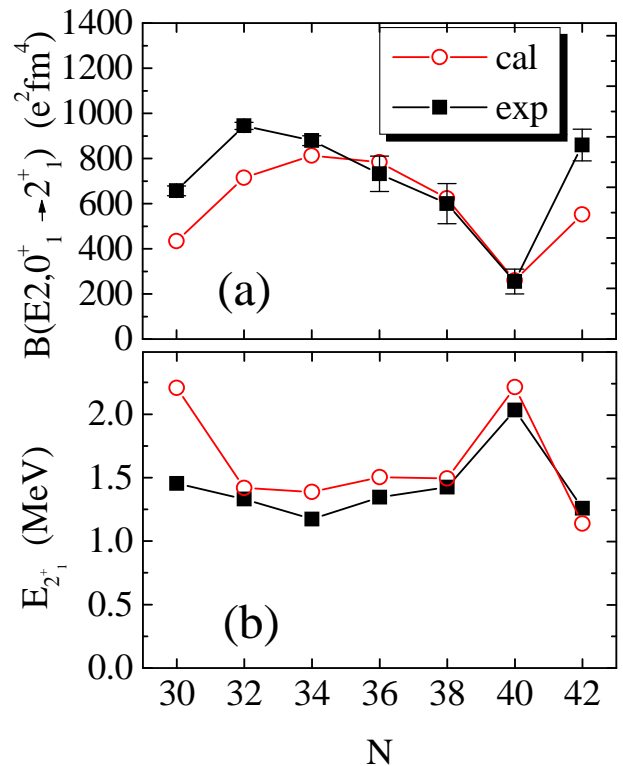


FIG. 1: (Color online) Comparison between the calculated and experimental values of (a)  $B(E2, 0_1^+ \rightarrow 2_1^+)$  and (b)  $E_{2_1^+}$  for the Ni isotopes. The calculated values are denoted by open circles and the experimental data [6, 9, 19, 20] by solid squares.

core-excitations from  $^{56}\text{Ni}$  are taken into account implicitly by the effective two-body matrix elements and the proton contributions are estimated from the KB3 calculations [21] in  $^{48}\text{Ca}$ . The neutron effective charge is taken as  $e_n = 1.0$  so as to reproduce the experimental  $B(E2, 0_1^+ \rightarrow 2_1^+)$  of  $^{68}\text{Ni}$  [17]. We use the VMS interaction starting from a realistic neutron G-matrix interaction based on the Bonn-C *NN* potential.

As one can see in Fig. 1, our calculations reproduce nicely the observed trends in  $B(E2, 0_1^+ \rightarrow 2_1^+)$  and  $E_{2_1^+}$  [17]. In particular, a large  $2_1^+$  excitation energy and small  $B(E2, 0_1^+ \rightarrow 2_1^+)$  value at  $N = 40$  are correctly obtained. It should be pointed out that the proton core excitations may significantly contribute to the excitation energy and to  $B(E2, 0_1^+ \rightarrow 2_1^+)$  in  $^{58}\text{Ni}$ , and thus it is difficult to absorb these effects into the effective interaction and the effective charges. In addition, the very recent observation [20] indicates a large  $B(E2, 0_1^+ \rightarrow 2_1^+)$  value in  $^{70}\text{Ni}$ , which exceeds the calculated one. Figure 2 shows two-neutron separation energy  $S_{2n}$  and the difference between two-neutron separation energies  $\delta_{2n}$ , defined respectively by

$$S_{2n}(Z, N) = B(Z, N) - B(Z, N - 2), \quad (2)$$

$$\delta_{2n}(Z, N) = S_{2n}(Z, N) - S_{2n}(Z, N + 2). \quad (3)$$

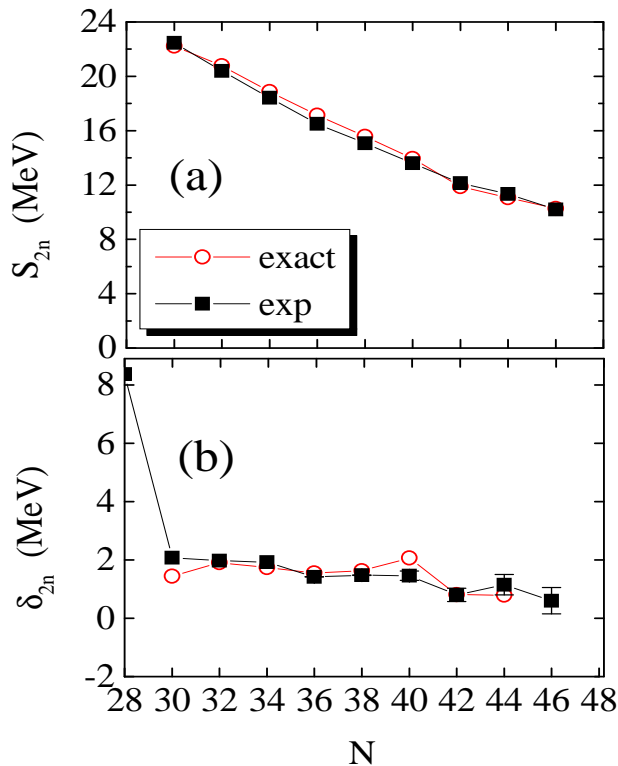


FIG. 2: (Color online) (a) Two-neutron separation energies and (b) differences between the two-neutron separation energies defined in Eq. (3). The exact shell-model results are denoted by open circles and the experimental data [19, 22] by solid squares.

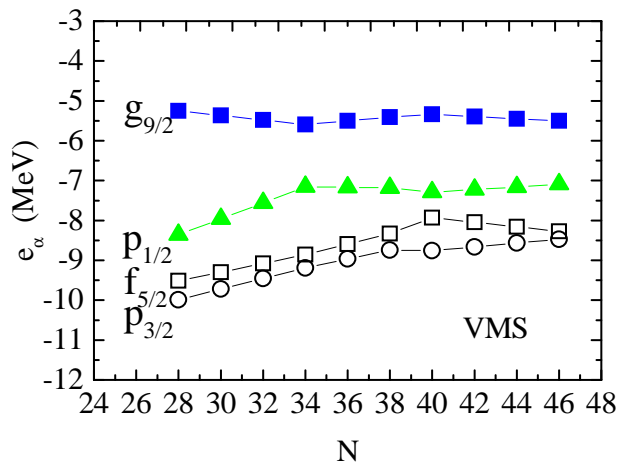


FIG. 3: (Color online) Spherical neutron shell structure. The HF single-particle energy levels  $e_\alpha$  predicted in the HF calculations with the VMS interaction for the Ni isotopes.

In Eq. (2),  $B(Z, N)$  is the binding energy taken as positive values. The quantity  $\delta_{2n}$  is known as the most sensitive and direct signature for a (sub)shell closure. Our shell model calculations reproduce well the experimental values of  $S_{2n}$  and  $\delta_{2n}$ . As can be seen in Fig. 2,  $S_{2n}$  and  $\delta_{2n}$  are smooth functions, and in particular, do not show

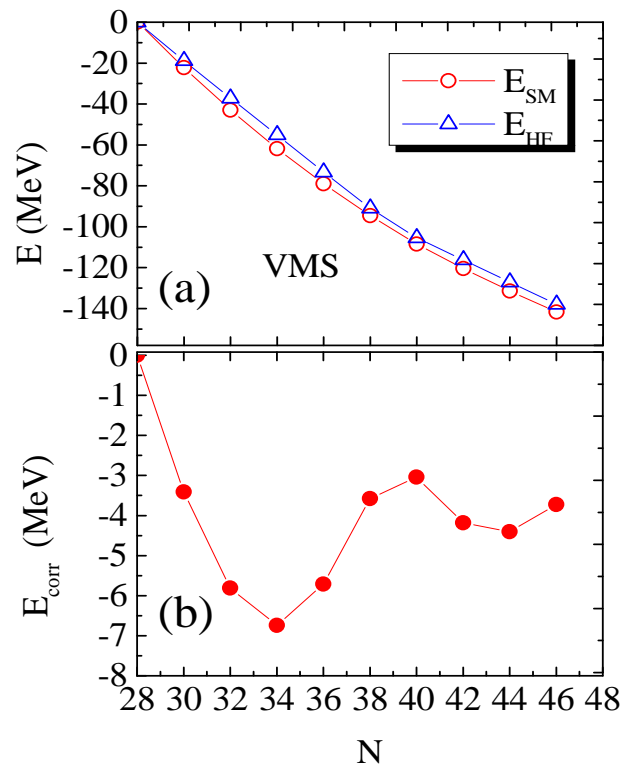


FIG. 4: (Color online) (a) Total energies and (b) correlation energies in the shell-model and the HF calculations with the VMS interaction for the Ni isotopes. Note that the absolute correlation energies become small around  $N = 40$ .

any notable changes at  $N = 40$ . Thus,  $^{68}\text{Ni}$  has a large  $E_{2_1^+}$  and a small  $B(E2, 0_1^+ \rightarrow 2_1^+)$ , but no irregularity in  $S_{2n}$  and no strong peak in  $\delta_{2n}$ . It is therefore very interesting to further look into the  $S_{2n}$  and  $\delta_{2n}$  results from the viewpoint of the magicity in  $^{68}\text{Ni}$ .

Let us analyze the shell-model results in Fig. 2 using mean-field procedures. We carry out Hartree-Fock (HF) and Hartree-Fock-Bogolyubov (HFB) calculations using the shell-model Hamiltonian (1). In the calculations, we impose spherical symmetry. The HF single-particle energies are given by

$$e_\alpha = \varepsilon_\alpha + \sum_{\beta=\text{occup}} V_{\alpha\beta,\alpha\beta}, \quad (4)$$

where  $\sum_{\beta=\text{occup}}$  means the summation over the occupied states only. Figure 3 shows the HF single-particle energies  $e_\alpha$ . The single-particle energy gap between  $g_{9/2}$  and  $fp$ -shell varies from 4 MeV at  $N = 28$  to 2.5 MeV at  $N = 40$ , which shows a persistence of a large shell gap at this neutron number. As we shall discuss below, this gap in the static single-particle picture will be washed out by dynamic correlations.

The total HF energy is expressed as

$$E_{\text{HF}} = \sum_{\alpha} \left( \varepsilon_\alpha + \frac{1}{2} \sum_{\beta=\text{occup}} V_{\alpha\beta,\alpha\beta} \right). \quad (5)$$

On the other hand, the HFB approximation is carried out with the following procedure. The HFB transformation is given by

$$a_{\alpha}^{\dagger} = u_{\alpha}c_{\alpha}^{\dagger} - v_{\alpha}c_{\bar{\alpha}}, \quad (6)$$

where  $\bar{\alpha}$  is the time reversed state to  $\alpha$  and the occupation numbers  $v_{\alpha}^2$  satisfy the following equation

$$v_{\alpha}^2 = \frac{1}{2} \left( 1 - \frac{\tilde{\epsilon}_{\alpha} - \lambda}{\sqrt{(\tilde{\epsilon}_{\alpha} - \lambda)^2 + \Delta_{\alpha}^2}} \right). \quad (7)$$

Here the self-consistent mean-fields, the self-consistent pairing gaps, and the canonical single-particle energies are respectively defined as

$$\Gamma_{\alpha} = \sum_{\beta} V_{\alpha\beta,\alpha\beta} v_{\beta}^2, \quad (8)$$

$$\Delta_{\alpha} = \sum_{\beta} V_{\alpha\bar{\alpha},\beta\bar{\beta}} u_{\beta} v_{\beta}, \quad (9)$$

$$\tilde{\epsilon}_{\alpha} = \epsilon_{\alpha} + \Gamma_{\alpha}, \quad (10)$$

and the total HFB energy [23] is

$$E_{\text{HFB}} = \sum_{\alpha} \left[ (\epsilon_{\alpha} + \frac{1}{2}\Gamma_{\alpha})v_{\alpha}^2 - \frac{1}{2}\Delta_{\alpha}u_{\alpha}v_{\alpha} \right]. \quad (11)$$

The neutron chemical potential  $\lambda$  is determined by the neutron number conservation

$$\sum_{\alpha} v_{\alpha}^2 = N. \quad (12)$$

Eqs. (7) and (12) are solved iteratively. In this paper, however, we get the solutions by minimizing the total HFB energy (11) with the neutron number conservation (12) under the normalization condition  $u_{\alpha}^2 + v_{\alpha}^2 = 1$ .

The total shell-model energies  $E_{\text{SM}}$  and the HF energies  $E_{\text{HF}}$  are plotted in Fig. 4(a), and the correlation energies, defined as  $E_{\text{corr}} = E_{\text{SM}} - E_{\text{HF}}$ , are shown in Fig. 4(b). The correlation energy exhibits a characteristic pattern where the absolute value is the largest at  $N = 34$  but has a local minimum at  $N = 40$ . The reduction in correlation energy at  $N = 40$  would be attributed to the small pairing gap  $\Delta_{1/2}$  of the  $p_{1/2}$  orbit with a small  $j$ .

Calculations for two-neutron separation energy  $S_{2n}$  and the difference between two-neutron separation energies  $\delta_{2n}$  are shown in Fig. 5. One can clearly see the irregularity in  $S_{2n}$  and a peak in  $\delta_{2n}$  in the HF calculation for  $^{68}\text{Ni}$ , which suggest a large energy gap and a subshell closure at  $N = 40$ . This result is consistent with the most of the Skyrme HF (SHF) and relativistic mean-field (RMF) calculations, which produced a distinct  $\delta_{2n}$  peak at  $N = 40$  [10, 11]. However, as seen in Fig. 5, the irregularity in  $S_{2n}$  and peak in  $\delta_{2n}$  do not show up in the HFB calculations when the  $T = 1, J = 0$  pairing interaction is included. We may therefore conclude that

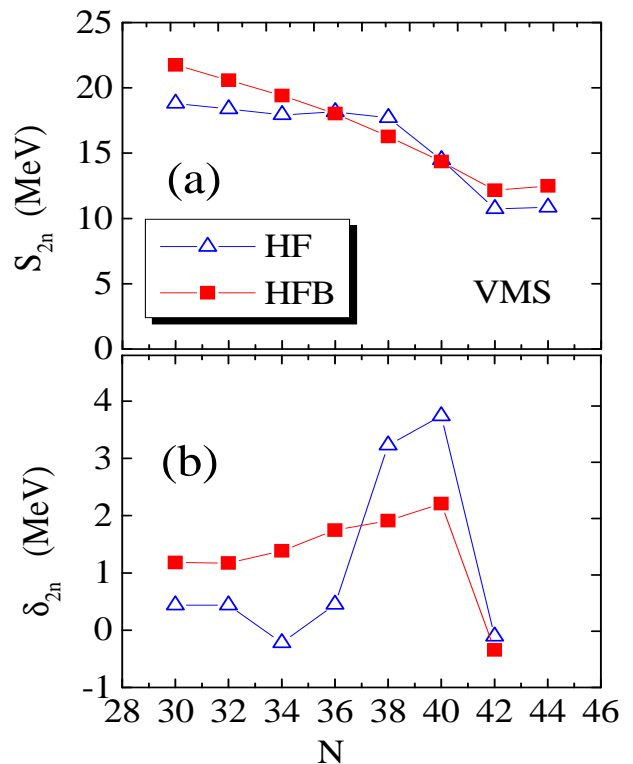


FIG. 5: (Color online) (a) Calculated two-neutron separation energies and (b) differences between the two-neutron separation energies defined by Eq. (3) in the mean-field approximation using the VMS interaction. The HF results are denoted by open triangles and the HFB ones by solid squares. Note that at  $N = 40$  irregularity of  $S_{2n}$  appears in the HF calculation and disappears in the HFB calculation.

the  $T = 1, J = 0$  pairing interaction is responsible for the observed smooth behavior in  $S_{2n}$  and  $\delta_{2n}$ , and thus for the disappearance of a magicity character in  $^{68}\text{Ni}$ . This conclusion is different from that of the SHF and RMF calculations in which the disappearance of the  $\delta_{2n}$  peak is caused by quadrupole correlations [10, 11].

The above conclusion is reinforced by the following analysis. To see the role of the  $T = 1, J = 0$  pairing interaction in the shell model calculations, we divide the two-body interaction  $H_{\text{int}}$  in the total Hamiltonian (1) into two parts

$$H_{\text{int}} = H_{J=0} + H_{J>0}, \quad (13)$$

where  $H_{J=0}$  is the  $T = 1, J = 0$  pairing interaction and  $H_{J>0} = H - H_{J=0}$ . Figure 6 compares different calculations for  $S_{2n}$  and  $\delta_{2n}$ . We evaluate  $S_{2n}$  and  $\delta_{2n}$  by using the binding energy  $B(Z, N)$  calculated from the expectation values  $\langle H - H_{J=0} \rangle$  and  $\langle H - H_{J>0} \rangle$ , and compare them with the results of the full Hamiltonian. All these calculations use the same ground-state wavefunction obtained from diagonalization of the total Hamiltonian (1). Now the significant role of the  $T = 1, J = 0$  pairing interaction is clearly shown: when  $H_{J=0}$  is switched off,  $S_{2n}$  exhibits irregularity and a large peak in  $\delta_{2n}$  is seen

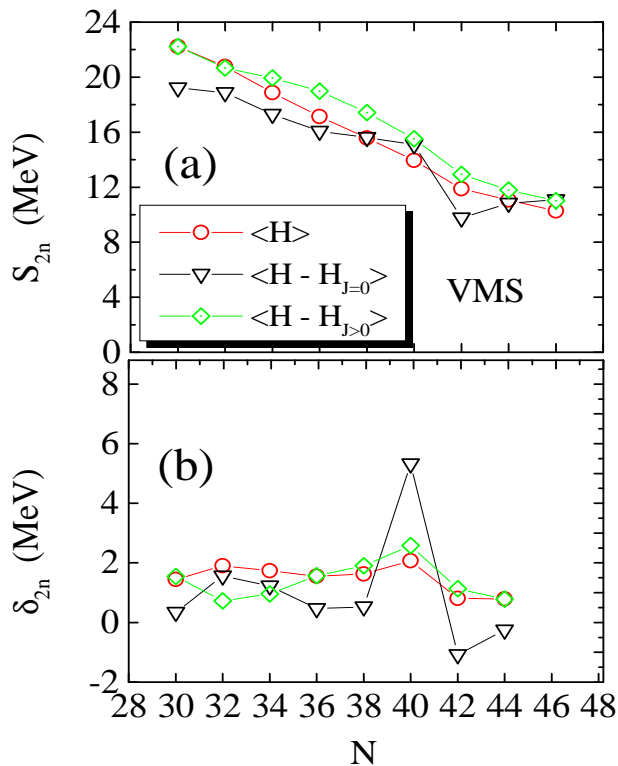


FIG. 6: (Color online) (a) Two-neutron separation energies and (b) differences between the two-neutron separation energies defined by Eq. (3) from the shell-model calculations using the VMS interaction. The exact shell-model results are denoted by open circles, the expectation values neglecting the  $T = 1, J = 0$  interactions by open triangles, and the expectation values neglecting the  $J > 0$  interactions by open diamonds. Note that only the  $\langle H - H_{J=0} \rangle$  result shows irregularity at  $N = 40$ .

at  $N = 40$ , whereas in  $\langle H - H_{J>0} \rangle$ , no irregularity in  $S_{2n}$  and no peak in  $\delta_{2n}$  can be seen.

In Fig. 7, we further examine the expectation values for various Hamiltonian terms. For the quantity  $\langle H_{J=0} \rangle$ , one sees that the contribution of the  $T = 1, J = 0$  pairing causes a bending at  $N = 40$ . On the other hand,  $\langle H_{J>0} \rangle$  increases monotonously with  $N$ . The total expectation value  $\langle H_{int} \rangle$  in Fig. 7 corresponds to the correlation energy in Fig. 4 (b). Thus we have understood the source of the seeming irregularity in  $S_{2n}$  and the peak in  $\delta_{2n}$  (see Fig. 5). The irregularity shows up in two-neutron separation energy at  $N = 40$  if the  $T = 1, J = 0$  pairing interaction is missing. Inclusion of the  $T = 1, J = 0$  pairing interaction washes out the irregularities in  $S_{2n}$  and  $\delta_{2n}$  found in the HF calculations, and thus explains the observations. It was inferred from the discussion of the  $g_{9/2}$  occupation number that the erosion of the  $N = 40$  shell gap is attributed to the pairing correlations [9].

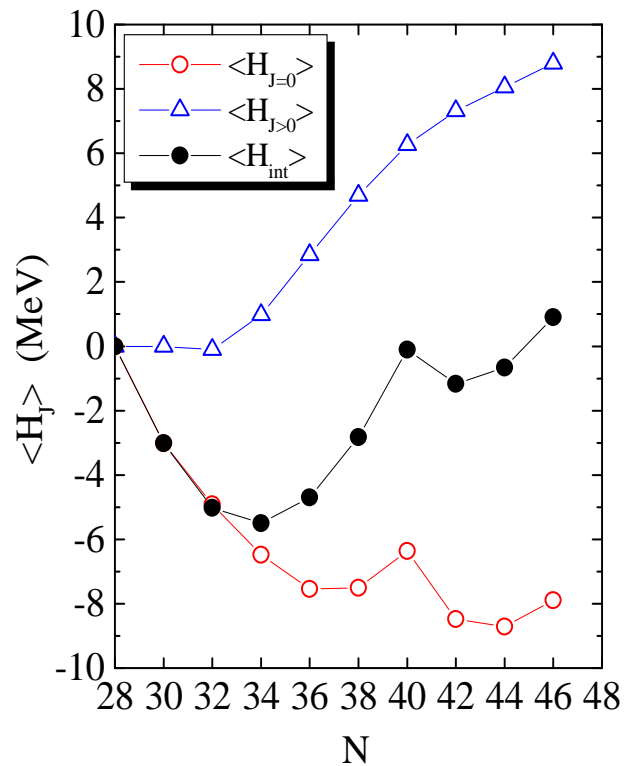


FIG. 7: (Color online) Expectation values of  $H_{J=0}$  and  $H_{J>0}$  in Eq. (13), which are denoted by open circles and open triangles, respectively. The total interaction energy  $\langle H_{int} \rangle$  is also depicted by solid circles. Note that  $\langle H_{J=0} \rangle$  displays a bending at  $N = 40$ .

## B. Level structure in $^{64-68}\text{Ni}$

In this section, we discuss the structure evolution along the isotopic chain  $^{64-68}\text{Ni}$ . Figure 8 shows the experimental and theoretical level schemes. The  $B(E2)$  values have been measured only for the first transition between the  $2_1^+$  state and the ground state [19]. Since in  $^{64}\text{Ni}$ , the  $0_2^+, 2_2^+$ , and  $4_1^+$  states all lie around 2.7 MeV and their excitation energies are approximately twice the first excited  $2_1^+$  energy ( $\sim 1.38$  MeV), the level sequence appears to be consistent with that of an harmonic vibration. This sequence is typical for low-lying excitations in spherical nuclei. Anharmonicity of the 2-phonon states ( $0_2^+, 2_2^+, 4_1^+$ ) becomes large in  $^{66}\text{Ni}$ , and the harmonic pattern breaks down completely in  $^{68}\text{Ni}$  where the  $0_2^+$  level drops down, and appears below the  $2_1^+$  level.

We carry out shell-model calculations using the VMS interaction. The results are compared with data in Fig. 8 and the predicted  $B(E2)$  values are summarized in Table I. The calculations can well reproduce the experimental energy levels and the  $B(E2, 0_1^+ \rightarrow 2_1^+)$  values, and the systematic behavior of the low-lying  $0_2^+$  state is also reasonably described. It is striking that in our results, an excited band is formed in  $^{68}\text{Ni}$  based on the  $0_2^+$  state. The  $E2$  transition probability  $B(E2, 0_2^+ \rightarrow 2_1^+)$  is quite small in  $^{64,66}\text{Ni}$ , but becomes rather large in  $^{68}\text{Ni}$ . The

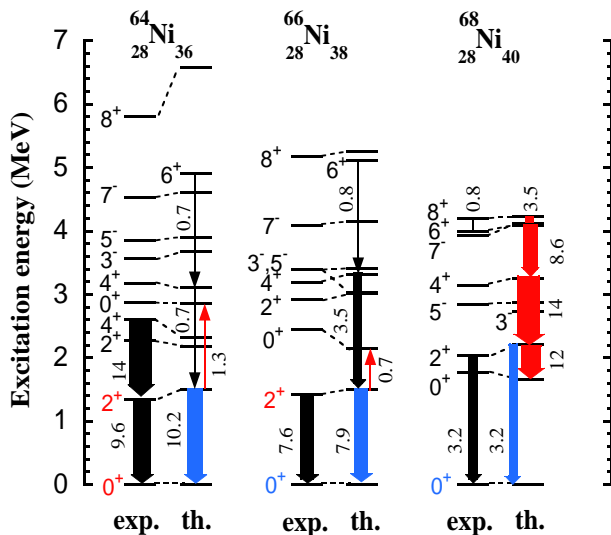


FIG. 8: (Color online) Comparison between the theoretical and experimental level scheme [6, 9, 19] for  $^{64-68}\text{Ni}$ . The widths of the arrows denote relative values of  $B(E2)$ . The numbers by the arrows are the  $B(E2)$  values in Weisskopf units.

values  $B(E2, 4_1^+ \rightarrow 2_1^+)$  and  $B(E2, 6_1^+ \rightarrow 4_1^+)$  in  $^{68}\text{Ni}$  are also large. In contrast,  $B(E2, 0_1^+ \rightarrow 2_1^+)$  in  $^{68}\text{Ni}$  is found smaller than those in  $^{64,66}\text{Ni}$ . Thus we have predicted a new band in  $^{68}\text{Ni}$ , as shown in Fig. 8.

In order to see how this band is formed, we compare neutron occupation numbers of the  $p_{3/2}$ ,  $f_{5/2}$ ,  $p_{1/2}$ , and  $g_{9/2}$  orbits in the relevant low-lying states in  $^{66}\text{Ni}$  and  $^{68}\text{Ni}$ . As one can see in Fig. 9, except for the  $6_1^+$  state, neutron occupation numbers in the low-lying states in  $^{66}\text{Ni}$  are dominated by the  $fp$ -shell components. This is because the Fermi energy of  $^{66}\text{Ni}$  lies below the  $p_{1/2}$  orbit. However, neutron occupation numbers in  $^{68}\text{Ni}$  show very different values [9]. Except for the ground state, occupation number of the  $g_{9/2}$  orbit in all low-lying states in  $^{68}\text{Ni}$  increases by more than two units. This means that two neutrons are excited from the  $fp$ -shell to the  $g_{9/2}$

TABLE I:  $B(E2)$  values for the positive-parity yrast states and some excited states in  $^{66}\text{Ni}$  and  $^{68}\text{Ni}$ . The calculated values are the shell-model results using the VMS interaction. Data are taken from Refs. [6, 9, 19].

$I_i^\pi \rightarrow I_f^\pi$	$^{66}\text{Ni}$ [ $e^2\text{fm}^4$ ]		$^{68}\text{Ni}$ [ $e^2\text{fm}^4$ ]	
	exp	cal	exp	cal
$2_1^+ \rightarrow 0_1^+$	120(20)	125	53(12)	52
$4_1^+ \rightarrow 2_1^+$		56		239
$6_1^+ \rightarrow 4_1^+$		13		144
$8_1^+ \rightarrow 6_1^+$		79	26(1)	58
$2_1^+ \rightarrow 0_2^+$		11		198
$2_2^+ \rightarrow 0_1^+$		12		15
$2_2^+ \rightarrow 2_1^+$		12		36
$2_2^+ \rightarrow 0_2^+$		14		27

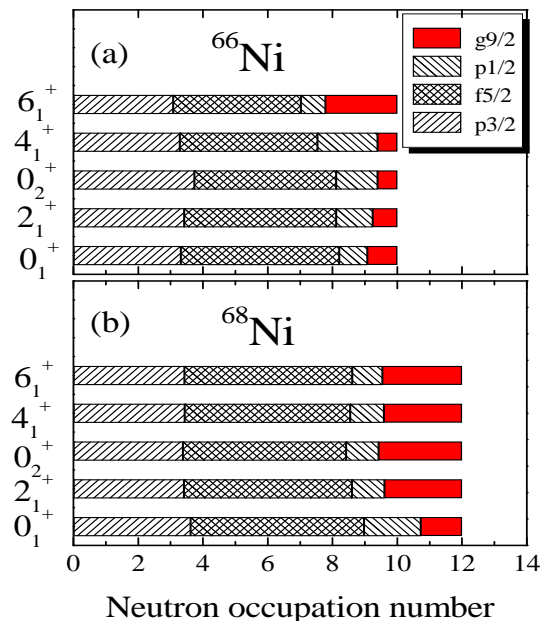


FIG. 9: (Color online) Neutron occupation numbers of the  $fp$ -shell orbits for the low-lying levels in (a)  $^{66}\text{Ni}$  and (b)  $^{68}\text{Ni}$ .

orbit in these states in  $^{68}\text{Ni}$  [11, 24]. To see the structure of the low-lying states more clearly, we calculate the probability of  $n$ -particle- $n$ -hole ( $np$ - $nh$ ) excitations from the  $fp$ -shell to the  $g_{9/2}$  orbit, defined by

$$P_n = \frac{\langle N_n \rangle}{\sum_n \langle N_n \rangle}, \quad (14)$$

where  $N_n$  are the  $np$ - $nh$  operators from the  $fp$ -shell to the  $g_{9/2}$  orbit. Table II lists the probabilities of  $np$ - $nh$  excitations in the relevant low-lying states of  $^{66}\text{Ni}$  and  $^{68}\text{Ni}$ . In  $^{66}\text{Ni}$ , in all low-lying states except the  $6_1^+$  state, the dominant components are the  $0p$ - $0h$  excitations but with considerable mixing of the  $2p$ - $2h$  excitations. The  $4p$ - $4h$  excitations are quite small in these states. The  $6_1^+$  state in  $^{66}\text{Ni}$  has almost a pure  $2p$ - $2h$  component. In contrast, the low-lying excited states in  $^{68}\text{Ni}$  show very different structures. While the ground state has mixed  $2p$ - $2h$  and  $0p$ - $0h$  components with nearly equal probability, the low-lying excited states have mainly the  $2p$ - $2h$  component with considerable mixing with the  $4p$ - $4h$  excitation. A large  $E_{2_1^+}$  and a small  $B(E2, 0_1^+ \rightarrow 2_1^+)$  in  $^{68}\text{Ni}$  (see Fig. 1) would be alternatively explained as follows. Once the odd-parity  $fp$  orbits are filled at  $N = 40$ , at least two-neutrons have to jump to the intruder  $g_{9/2}$  orbit to create a  $2_1^+$  state, and therefore the energy  $E_{2_1^+}$  increases [11, 17, 24]. The  $E2$  transition between  $2_1^+$  and  $0_1^+$  in  $^{68}\text{Ni}$  becomes small just because the two states have

TABLE II: Probabilities of  $n$  particle-hole excitations for the low-lying states of  $^{66}\text{Ni}$  and  $^{68}\text{Ni}$ .

$I^\pi$	$^{66}\text{Ni}$			$^{68}\text{Ni}$		
	0p-0h	2p-2h	4p-4h	0p-0h	2p-2h	4p-4h
$0_1^+$	0.596	0.347	0.054	0.482	0.405	0.104
$2_1^+$	0.654	0.311	0.034	0.000	0.728	0.254
$0_2^+$	0.718	0.260	0.022	0.108	0.610	0.256
$4_1^+$	0.715	0.262	0.023	0.000	0.800	0.009
$6_1^+$	0.000	0.891	0.107	0.000	0.779	0.210

different structure. Interestingly, we indeed see from our calculation that the band is built on the  $0_2^+$  state. This happens because all the excited states belonging to this band have a similar structure with the 2p-2h excitations.

In order to visualize the shape of  $^{68}\text{Ni}$ , we use the CHF method with the following quadratic constraint [15]

$$H' = H + \alpha \sum_{\mu} (\langle Q_{2\mu} \rangle - q_{\mu})^2 + \beta (\langle J_x \rangle - j_x)^2, \quad (15)$$

where  $Q_{2\mu}$  and  $J_x$  are the isoscalar quadrupole operators and the  $x$ -component of angular momentum operator, respectively. The  $q_{\mu}$ 's are constant parameters:  $q_0 = \sqrt{\frac{5}{16\pi}} q \cos\gamma$ ,  $q_{\pm 2} = \sqrt{\frac{5}{16\pi}} q \sin\gamma$ , and  $q_{\pm 1} = 0$ , where  $q$  is the isoscalar intrinsic quadrupole moment and  $\gamma$  is the triaxial angle. We set  $j_x = \sqrt{J(J+1)}$  with  $J$  the total angular momentum of the state. The parameters,  $\alpha$  and  $\beta$ , are taken so as to achieve a convergence for an iteration calculation with the gradient method. Then, potential energy surface (PES) is defined as the expectation value  $\langle H \rangle$  with respect to the CHF state for given  $q$  and  $\gamma$ . Figure 10 shows the contour plot of the PES in the  $q$ - $\gamma$  plane for  $^{68}\text{Ni}$ . We find that the PES minimum exhibits a spherical shape and an oblate softness. This is consistent with our previous discussions on the shell-model results, namely, a large  $E_{2_1^+}$  and a small  $B(E2, 0_1^+ \rightarrow 2_1^+)$  in  $^{68}\text{Ni}$ . The PES figure in Fig. 10 is in contrast to the characteristic feature of an oblate-prolate shape-coexistence in  $^{68}\text{Se}$  [25, 26].

### III. $N = 50$ ISOTONES

#### A. Magicity in $^{90}\text{Zr}$

In the previous section, we have discussed several unusual properties found in  $^{68}\text{Ni}$ , which are associated with the subshell closure at  $N = 40$ . A related question is how neutron-rich nuclei with  $Z = 40$  behave. Figure 11 shows the experimental  $B(E2, 0_1^+ \rightarrow 2_1^+)$  and the first excited  $2_1^+$  energy as a function of proton number  $Z$ , for some  $N = 50$  isotones. For both  $B(E2, 0_1^+ \rightarrow 2_1^+)$  and  $E_{2_1^+}$  values in Fig. 11, we find remarkable similarities as seen in Fig. 1: with increasing proton number

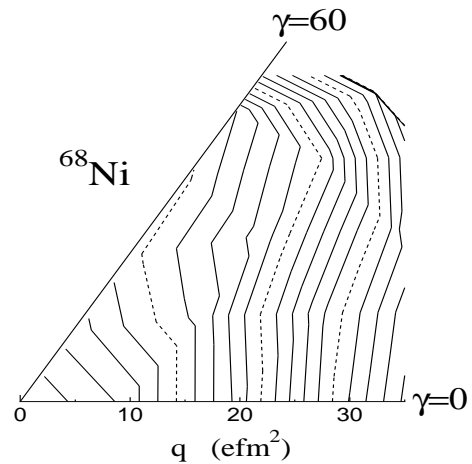


FIG. 10: Contour plot of PES on  $q - \gamma$  plane in the CHF calculation for  $^{68}\text{Ni}$ .

$Z$ ,  $B(E2)$  quickly increases until  $Z = 34$  and then decreases from  $Z = 36$  to  $Z = 40$ . The first excited  $2_1^+$  energy  $E_{2_1^+}$  goes up gradually and is peaked at  $Z = 40$ . Again, in terms of  $B(E2, 0_1^+ \rightarrow 2_1^+)$  and  $E_{2_1^+}$ ,  $^{90}\text{Zr}$  seems to be a double-magic nucleus. It should be pointed out that  $B(E2, 4_1^+ \rightarrow 2_1^+)$  shows different behavior from  $B(E2, 0_1^+ \rightarrow 2_1^+)$  [28]. Recent lifetime measurements for  $^{96}\text{Pd}$  and  $^{94}\text{Ru}$  corroborate the tendency of this behavior for  $N = 50$  [29]. Moreover, it has been shown recently that the exact strengths for these transitions cannot be reproduced in a  $T = 1$  model space but require neutron excitations across the  $N = 50$  shell [30].

We carry out shell-model calculations for the  $N = 50$  isotones. Since  $^{78}\text{Ni}$  is taken as a core, the model space for proton is restricted to the  $fp$ -shell, and the neutrons are assumed to be inactive. The proton effective charge is taken as  $e_p = 1.8$  for the VMS interaction and  $e_p = 2.0$  for the JW interaction so as to reproduce the experimental  $B(E2, 0_1^+ \rightarrow 2_1^+)$  value of  $^{90}\text{Zr}$  [17]. We use two types of effective interactions: the proton part of the VMS interaction and the JW interaction. As one can see in Fig. 11, the calculations nicely reproduce the observed trends for both  $B(E2, 0_1^+ \rightarrow 2_1^+)$  and  $E_{2_1^+}$ .

Figure 12 shows the two-proton separation energy  $S_{2p}$  and the difference between two-proton separation energies  $\delta_{2p}$  for this isotonic chain, defined by

$$S_{2p}(Z, N) = B(Z, N) - B(Z - 2, N), \quad (16)$$

$$\delta_{2p}(Z, N) = S_{2p}(Z, N) - S_{2p}(Z + 2, N). \quad (17)$$

The experimental data do not show a signature for a subshell closure in  $^{90}\text{Zr}$ , since no irregularity in  $S_{2p}$  can be seen. The shell-model calculations reproduce well the experimental values of  $S_{2p}$ . In particular, the small peak in  $\delta_{2p}$  at  $N = 38$  is well described. To understand these results, we analyze the role of the  $T = 1, J = 0$  pairing interaction ( $H_{J=0}$ ) and the other interactions ( $H_{J>0}$ ) in the Hamiltonian, as done in the previous section (see Eq. (13)). In contrast to the case of the Ni isotopes,

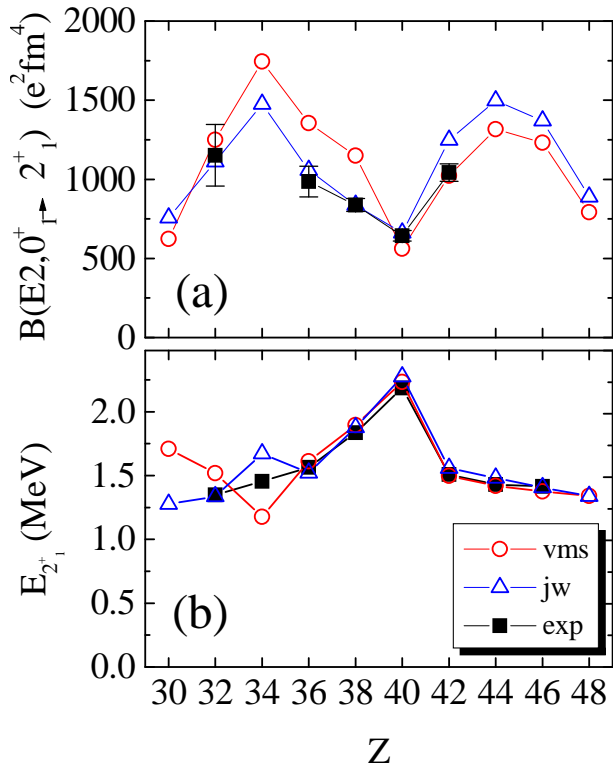


FIG. 11: (Color online) Comparison between the calculated and experimental values of (a) the  $B(E2, 0^+ \rightarrow 2^+)$  and (b)  $E_{2^+}$  for  $N = 50$  isotones. Data are taken from Refs. [16, 19, 27]. The shell-model calculations are carried out using the VMS and JW interactions. The calculated results are denoted by open circles (triangles) for the VMS (JW) interaction, and the experimental ones by solid squares.

Figs. 12(a) and Fig. 13(a) indicate that, while the  $T = 1, J = 0$  pairing interaction scarcely contributes to  $S_{2p}$ , the remaining interactions  $H_{J>0}$  increases  $S_{2p}$  significantly. Thus, the  $J > 0$  interactions are more important for two-proton separation energy in the  $N = 50$  isotones. The  $H_{J>0}$  contribution, however, does not produce any notable irregularity in  $S_{2p}$ . For  $\delta_{2p}$ , we can see some differences between the VMS and JW interactions in Figs. 12(b) and 13(b). Moreover, the  $H_{J=0}$  and  $H_{J>0}$  contributions to  $\delta_{2p}$  in the VMS results are different from those in the JW results.

Figure 14 shows the expectation values of  $H_{J=0}$ ,  $H_{J>0}$  and the total interaction energy  $\langle H_{int} \rangle$ . Comparing Fig. 14 with Fig. 7, we find that in the  $N = 50$  isotones,  $\langle H_{J>0} \rangle$  increases drastically with increasing proton number, and becomes dominant when  $Z$  is large. There is no clear bending at  $Z = 40$  in either curve  $\langle H_{J=0} \rangle$  and  $\langle H_{J>0} \rangle$ . Thus these detailed results have explained the trends of two-proton separation energy in Fig. 12(a) and Fig. 13(a).

Let us now study the contributions from the above interactions to HF single-particle energies  $e_\alpha$  in the HF, HF+BCS, and HFB treatments. We also evaluate two-proton separation energy  $S_{2p}$  within these treatments.

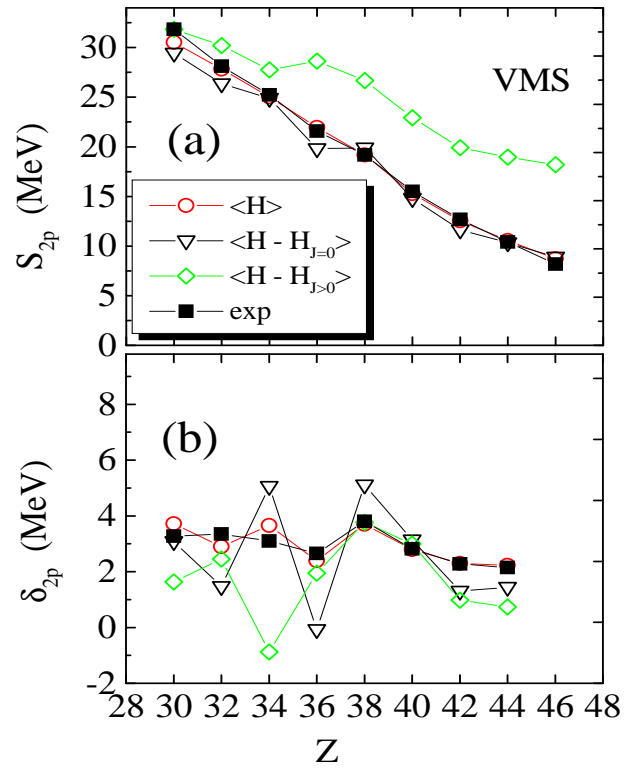


FIG. 12: (Color online) Two-proton separation energies in the shell-model calculations with the VMS interaction. The exact shell model results are denoted by open circles, the expectation values neglecting the  $T = 1, J = 0$  interactions by the open triangles, and the expectation values neglecting the  $J > 0$  interactions by the open diamonds. Experimental data [19, 22] are denoted by solid squares.

Figures 15 and 16 show respectively the results calculated with the VMS and JW interactions. It is seen that in the VMS results shown in Fig. 15(a), the single-particle energy gap between  $g_{9/2}$  and  $p_{1/2}$  orbits decreases quickly with increasing proton number. This causes a smooth variation in  $S_{2p}$  as seen in Fig. 15(b). All the HF type calculations do not produce irregularity in  $S_{2p}$ . In the JW results in Fig. 16(a), the single-particle energy gap between the  $g_{9/2}$  and  $p_{1/2}$  orbits remains large up to  $Z = 36$ , but becomes small after  $Z = 38$ . The Fermi energy, as found in all HF type calculations, lies in the  $fp$ -shell for  $Z = 30 - 38$ , and between  $g_{9/2}$  and  $p_{1/2}$  for  $Z = 40 - 46$ . Therefore, protons do not encounter a large energy gap when they are excited. Therefore, also with the JW interaction, irregularity in  $S_{2p}$  is not produced (see Fig. 16(b)). We note that in both Figs. 15 and 16, the proton separation energies in the HFB calculations deviate from those of the other calculations when  $Z$  is large. Similar trend is obtained in the shell-model calculation without the  $J > 0$  interaction.

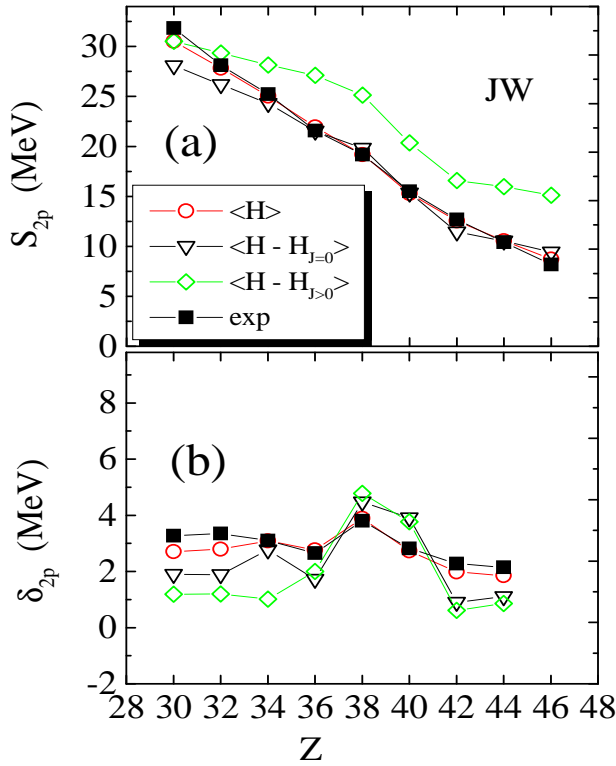


FIG. 13: (Color online) Same as Fig. 12, except that the calculations are performed by using the JW interaction.

### B. Level structure in $^{86}\text{Kr}$ , $^{88}\text{Sr}$ , and $^{90}\text{Zr}$

Experimental level schemes for  $^{86}\text{Kr}$ ,  $^{88}\text{Sr}$ , and  $^{90}\text{Zr}$  are shown in Figs. 17 and 18.  $B(E2)$  in these nuclei has been measured only for transitions between the  $2_1^+$  state and the ground state. Among the three isotones, the  $0_2^+$  level in  $^{90}\text{Zr}$  is the lowest in energy and lies below the  $2_1^+$  state. We perform shell-model calculations using the VMS and JW interactions, and the results are compared with data in Figs. 17 and 18 and the  $B(E2)$  values are summarized in Tables III and IV.

The calculations can reproduce the experimental energy levels and  $B(E2, 0_1^+ \rightarrow 2_1^+)$  values. In particular, the systematical behavior of the  $0_2^+$  state is well described. It is striking that the results show again an excited band in  $^{90}\text{Zr}$  based on the  $0_2^+$  state. For the  $E2$  transition probability  $B(E2, 0_2^+ \rightarrow 2_1^+)$ , both calculations indicate a quite small value in  $^{86}\text{Kr}$  and  $^{88}\text{Sr}$ , but a very large one in  $^{90}\text{Zr}$ . Moreover,  $B(E2, 4_1^+ \rightarrow 2_1^+)$  and  $B(E2, 6_1^+ \rightarrow 4_1^+)$  are found large in  $^{90}\text{Zr}$ . In contrast,  $B(E2, 0_1^+ \rightarrow 2_1^+)$  in  $^{90}\text{Zr}$  is smaller than that in  $^{86}\text{Kr}$  and  $^{88}\text{Sr}$ . All of these suggest strongly a new band in the  $Z = 40$  nucleus  $^{90}\text{Zr}$ .

To confirm the above findings, we further study the probability of the  $np$ - $nh$  excitations defined by Eq. (14),

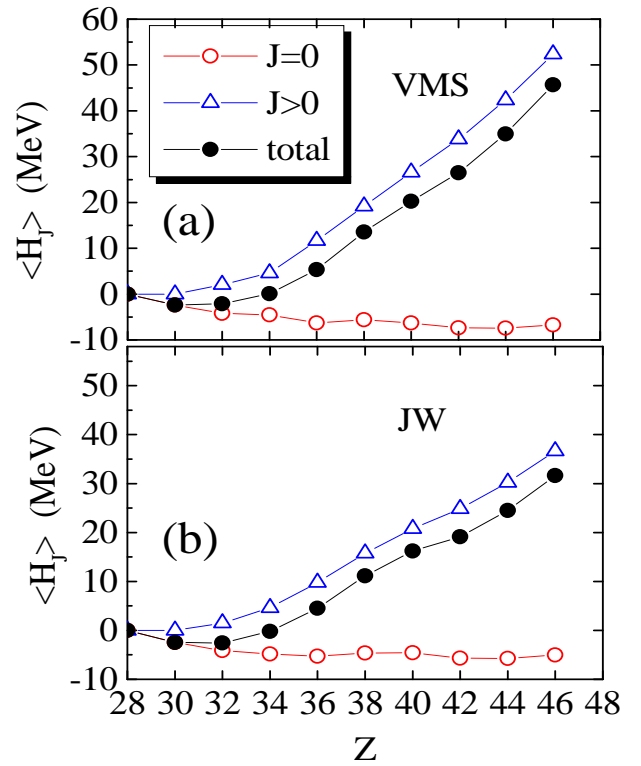


FIG. 14: (Color online) Expectation values of  $H_{J=0}$  and  $H_{J>0}$  defined by Eq. (13) for (a) the VMS interaction and (b) the JW interaction.  $\langle H_{J=0} \rangle$  and  $\langle H_{J>0} \rangle$  are denoted by open circles and open triangles, respectively. The total of them ( $\langle H_{int} \rangle$ ) is also depicted by solid circles. Note that the contributions of  $\langle H_{J>0} \rangle$  becomes large with increasing proton number.

in two shell-model calculations with the VMS and JW interactions. The results for  $^{88}\text{Sr}$  and  $^{90}\text{Zr}$  are listed in Tables V and VI, respectively. For  $^{88}\text{Sr}$  with the VMS interaction (Table V), the ground state and the  $2_1^+$  state have a dominant component of the  $0p$ - $0h$  excitation, and the  $0_2^+$  and  $4_1^+$  states have comparable probabilities of the  $0p$ - $0h$  and  $2p$ - $2h$  excitations. Note that the  $2_1^+$  state in

TABLE III:  $B(E2)$  values for the positive-parity yrast states and some excited states in  $^{88}\text{Sr}$  and  $^{90}\text{Zr}$ . Data are taken from Refs. [16, 19]. The calculated values are the shell-model results using the VMS interaction.

$I_i^\pi \rightarrow I_f^\pi$	$^{88}\text{Sr}$ [ $e^2\text{fm}^4$ ]		$^{90}\text{Zr}$ [ $e^2\text{fm}^4$ ]	
	exp	cal	exp	cal
$2_1^+ \rightarrow 0_1^+$	167(5)	230	129(4)	112
$4_1^+ \rightarrow 2_1^+$		113		277
$6_1^+ \rightarrow 4_1^+$		0.2	< 1054	180
$8_1^+ \rightarrow 6_1^+$		16	57(4)	65
$2_2^+ \rightarrow 0_2^+$		7.3	124(2)	240
$2_2^+ \rightarrow 0_1^+$	2.8(1)	0.5		38
$2_2^+ \rightarrow 2_1^+$		0.2		38
$2_2^+ \rightarrow 0_2^+$		0.1		133

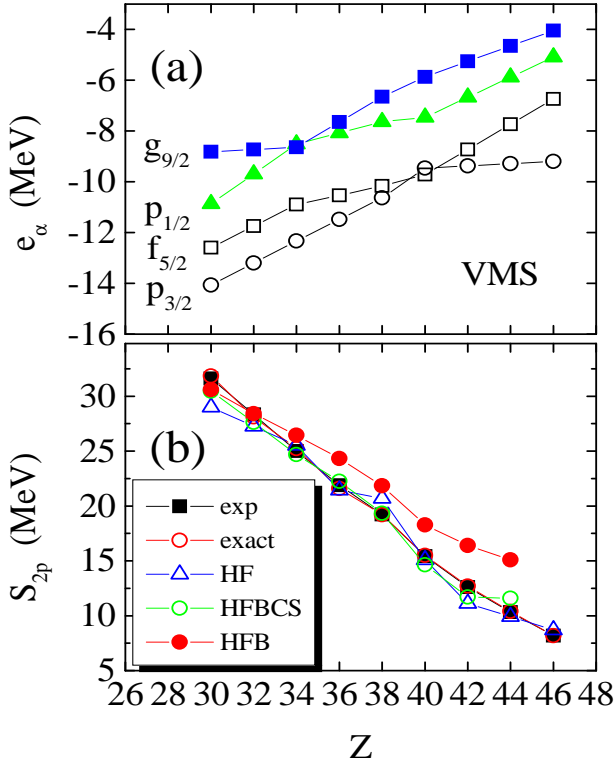


FIG. 15: (Color online) Spherical proton shell structure. (a) The HF single-particle energies  $e_\alpha$  obtained by the HF calculations with the VMS interaction and (b) the two-proton separation energies using the mean-field calculations for the  $N = 50$  isotones. The HF results are denoted by open triangles and the HFB ones the solid squares.

$^{88}\text{Sr}$  can be made by 1p-1h excitations from ( $f_{5/2}, p_{3/2}$ ) to  $p_{1/2}$ , which contribute to the  $E2$  transitions. In the JW results (Table VI), the 2p-2h components are dominant in the  $0_2^+$  and  $4_1^+$  states. The  $6_1^+$  state is almost a pure 2p-2h excitation in both VMS and JW interactions. One can thus expect that only the  $E2$  transition  $B(E2, 0_1^+ \rightarrow 2_1^+)$  is enhanced in  $^{88}\text{Sr}$ . In  $^{90}\text{Zr}$ , on the other hand, the ground state has the 0p-0h and 2p-2h components with nearly equal probability and the dominant components in the  $2_1^+$ ,  $0_2^+$ , and  $6_1^+$  states are the 2p-2h excitation

TABLE IV: Same as Table III, except that the calculations are performed by using the JW interaction.

$I_i^\pi \rightarrow I_f^\pi$	$^{88}\text{Sr} [e^2\text{fm}^4]$		$^{90}\text{Zr} [e^2\text{fm}^4]$	
	exp	cal	exp	cal
$2_1^+ \rightarrow 0_1^+$	167(5)	166	129(4)	133
$4_1^+ \rightarrow 2_1^+$		51		264
$6_1^+ \rightarrow 4_1^+$		116	< 1054	192
$8_1^+ \rightarrow 6_1^+$		226	57(4)	56
$2_1^+ \rightarrow 0_2^+$		70	124(2)	173
$2_2^+ \rightarrow 0_1^+$	2.8(1)	117		94
$2_2^+ \rightarrow 2_1^+$		23		0.05
$2_2^+ \rightarrow 0_2^+$		41		60

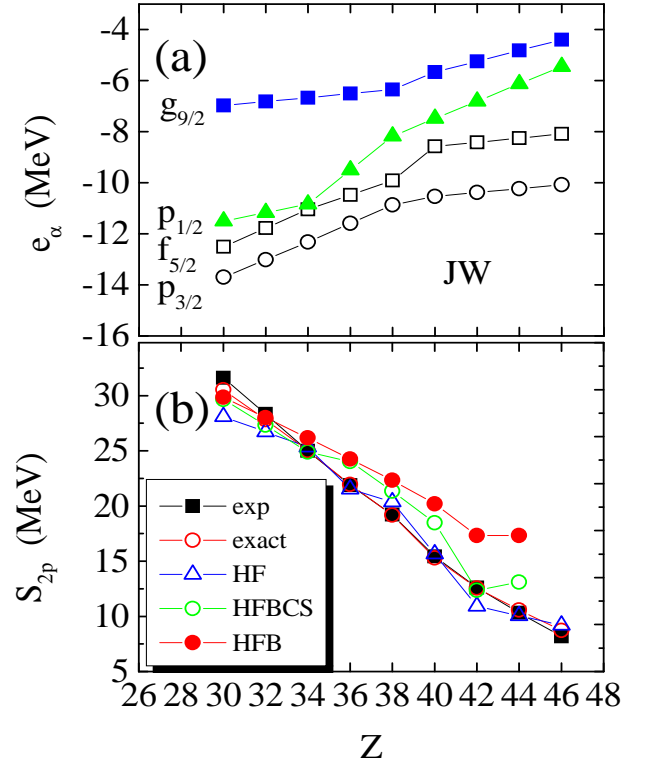


FIG. 16: (Color online) Same as Fig. 15, except that the calculations are performed by using the JW interaction.

TABLE V: Probabilities of  $np$ - $nh$  excitations in the low-lying states for  $^{88}\text{Sr}$  and  $^{90}\text{Zr}$ , where the VMS interaction is used in the shell-model calculations.

$I^\pi$	$^{88}\text{Sr}$			$^{90}\text{Zr}$		
	0p-0h	2p-2h	4p-4h	0p-0h	2p-2h	4p-4h
$0_1^+$	0.732	0.244	0.022	0.425	0.467	0.100
$2_1^+$	0.799	0.190	0.011	0.000	0.835	0.158
$0_2^+$	0.498	0.433	0.065	0.300	0.546	0.141
$2_2^+$	0.811	0.180	0.009	0.000	0.854	0.141
$4_1^+$	0.496	0.464	0.040	0.000	0.854	0.141
$6_1^+$	0.000	0.920	0.078	0.000	0.852	0.142

mixed with the 0p-0h component. Similar results are found in both calculations. From this analysis, we can understand that an excited band is formed on the  $0_2^+$  state in  $^{90}\text{Zr}$  because the  $0_2^+$ ,  $2_1^+$ ,  $4_1^+$ , and  $6_1^+$  states all have a similar structure with a large component of the 2p-2h excitations.

#### IV. CONCLUSIONS

We have studied the magicity of  $N$  or  $Z = 40$  and the level schemes for the neutron-rich nuclei  $^{68}\text{Ni}$  and  $^{90}\text{Zr}$  by means of the shell-model and the mean-field approximations. For both nuclei with either  $N = 40$  or  $Z = 40$ , their two-nucleon separation energies do not show any irregularity along the respective isotopic or isotonic chain,

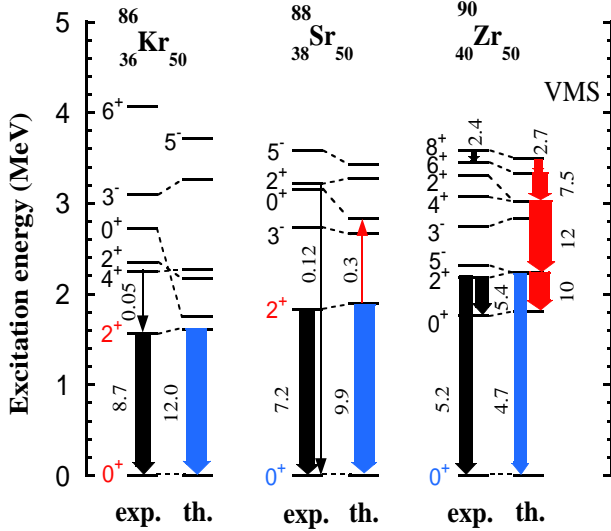


FIG. 17: (Color online) Comparison between the experimental and calculated level scheme for  $^{86}\text{Kr}$ ,  $^{88}\text{Sr}$ , and  $^{90}\text{Zr}$ . Data are taken from Refs. [16, 19]. The shell model calculations are carried out by using the VMS interaction. The widths of the arrows denote relative values of  $B(E2)$ . The numbers by the arrows are the  $B(E2)$  values in Weisskopf units.

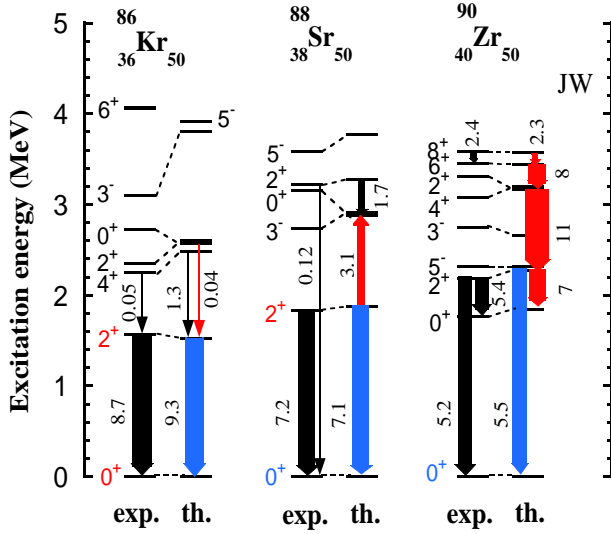


FIG. 18: (Color online) Same as Fig. 17, except that the theoretical results are obtained by using the JW interaction.

in spite of the apparent double-magic feature shown with a comparatively large  $2_1^+$  excitation energy and a small  $B(E2, 0_1^+ \rightarrow 2_1^+)$  value. The reason why the separation energy does not exhibit irregularity has been found different for the Ni isotopes and the  $N = 50$  isotones. From the shell-model calculations using the VMS and JW interactions, we have suggested that the  $T = 1, J = 0$  pairing interaction is responsible for the absence of any irregularity in separation energy in  $^{68}\text{Ni}$ . The irregularity appears in the HF treatment but disappears in the HFB treatment. This indicates that the shell gap at  $N = 40$

TABLE VI: Same as Table V, except that the calculations are performed by using the JW interaction.

$I^\pi$	$^{88}\text{Sr}$			$^{90}\text{Zr}$		
	0p-0h	2p-2h	4p-4h	0p-0h	2p-2h	4p-4h
$0_1^+$	0.809	0.184	0.006	0.452	0.484	0.062
$2_1^+$	0.899	0.100	0.001	0.000	0.894	0.104
$0_2^+$	0.208	0.729	0.061	0.356	0.523	0.115
$2_2^+$	0.671	0.320	0.013	0.000	0.925	0.074
$4_1^+$	0.250	0.714	0.036	0.000	0.904	0.094
$6_1^+$	0.000	0.967	0.032	0.000	0.912	0.087

disappears due to dynamical correlations of the isovector  $J = 0$  pairing interaction. In the case of  $^{90}\text{Zr}$ , however, irregularity in two-proton separation energy does not appear in the HF calculations. For the  $N = 50$  isotopes, the  $J > 0$  interactions contribute significantly to the two-proton separation energy.

We have also studied level schemes for  $^{68}\text{Ni}$  and  $^{90}\text{Zr}$ . We have predicted an excited band built on the  $0_2^+$  state in both nuclei. The dominant component of this band has been determined as the 2p-2h excitations from the  $fp$ -shell to the intruder  $g_{9/2}$  orbit. The structure of the excited states of this band is quite different from that of the ground state. This happens because the opposite signs of parity between the  $g_{9/2}$  orbit and the  $fp$ -shell do not allow 1p-1h excitations [24]. The first excited  $2_1^+$  state in  $^{68}\text{Ni}$  and  $^{90}\text{Zr}$  lies higher, and  $B(E2, 0_1^+ \rightarrow 2_1^+)$  is relatively weak. The difference in parity between the  $fp$  and the  $g_{9/2}$  subshells leads to a small probability of quadrupole excitations across  $N = 40$ , and the large energy gain due to pairing correlations in the  $g_{9/2}$  subshell is responsible for the high  $2^+$  energy in  $^{68}\text{Ni}$ .

[1] M. G. Mayer, Phys. Rev. **75**, 1947 (1949); O. Haxel, J. H. Jensen, and H. E. Suess, Phys. Rev. **75**, 1766 (1949).  
[2] K. Heyde, P. Van Isacker, M. Waroquier, J. L. Wood, and R. M. Meyer, Phys. Rep. **102**, 291 (1983).  
[3] J. L. Wood, K. Heyde, W. Nazarewicz, M. Huyse, and P. Van Duppen, Phys. Rep. **215**, 101 (1992).  
[4] T. Otsuka, R. Fujimoto, Y. Utsuno, B. A. Brown, M. Honma, and T. Mizusaki, Phys. Rev. Lett. **87**, 082502 (2001).  
[5] M. Yamagami and N. Van Giai, Phys. Rev. C **69**, 034301

(2004).  
[6] R. Broda, *et al.*, Phys. Rev. Lett. **74**, 868 (1995).  
[7] R. Grzywacz, *et al.*, Phys. Rev. Lett. **81**, 766 (1998).  
[8] T. Ishii, *et al.*, Eur. Phys. J. A **13**, 15 (2002).  
[9] O. Sorlin, *et al.*, Phys. Rev. Lett. **88**, 092501 (2002).  
[10] P. G. Reinhard, M. Bender, T. Buervenich, C. Reiss, J. Maruhn, and W. Greiner, REKIN Review, **26**, 23 (2000).  
[11] H. Grawe and M. Lewitowicz, Nucl. Phys. **A693**, 116 (2001).  
[12] K. Langanke, J. Terasaki, F. Nowacki, D. J. Dean, and

- W. Nazarewicz, Phys. Rev. C **67**, 044314 (2003).
- [13] D. Rudolph, *et al.*, Phys. Rev. Lett. **82**, 3763 (1999).
- [14] T. Otsuka, M. Honma, and T. Mizusaki, Phys. Rev. Lett. **81**, 1588 (1998).
- [15] T. Mizusaki, T. Otsuka, Y. Utsuno, M. Honma, and T. Sebe, Phys. Rev. C **59**, R1846 (1999).
- [16] P. E. Garrett, *et al.*, Phys. Rev. C **68**, 024312 (2003).
- [17] A. F. Lisetskiy, B. A. Brown, M. Horoi, and H. Grawe, Phys. Rev. C **70**, 044314 (2004).
- [18] X. Ji and B. H. Wildenthal, Phys. Rev. C **37**, 1256 (1988).
- [19] R. B. Firestone and V. S. Shirley, *Table of Isotopes*, 8th ed. (Wiley-Interscience, New York, 1996).
- [20] O. Perru *et al.*, Phys. Rev. Lett. **96**, 232501 (2006).
- [21] E. Caurier, A.P. Zuker, A. Poves, G. Martínez-Pinedo, Phys. Rev. C **50** (1994) 225; A. Poves, A.P. Zuker, Phys. Rep. **70** (1981) 235.
- [22] G. Audi and A. H. Wapstra, Nucl. Phys. **A595**, 409 (1995).
- [23] P.-G. Reinhard, D. J. Dean, W. Nazarewicz, J. Dobaczewski, J. A. Maruhn, and M. R. Strayer, Phys. Rev. C **60**, 014316 (1999).
- [24] H. Grawe *et al.*, Proc. TOURS 2000, AIP Conf. Proc., Vol. **561**, 2001, p287.
- [25] S. M. Fischer, D. P. Balamuth, P. A. Hausladen, C. J. Lister, M. P. Carpenter, D. Seweryniak, and J. Schwartz, Phys. Rev. Lett. **84**, 4064 (2000).
- [26] K. Kaneko, M. Hasegawa and T. Mizusaki, Phys. Rev. C **70**, 051301(R)(2004).
- [27] E. Padilla-Rodal *et al.*, Phys. Rev. Lett. **94**, 122501 (2005).
- [28] A. Lisetskiy *et al.*, Eur. Phys. J. **A25**, 95 (2005).
- [29] H. Mach *et al.*, Proc. Int. Symposium *A New Era of Nuclear Structure Physics*, Niigata, Japan 2003, eds. Y. Suzuki, S. Ohya, M Matsuo, T. Ohtubo, World Scientific, Singapore, 2004, p277.
- [30] H. Grawe, A. Blazhev, M. Gorska, R. Grzywacz, H. Mach, and I. Mukha, Eur. Phys. J. **A27**, 257 (2006).